



**University of  
Zurich**<sup>UZH</sup>

**Zurich Open Repository and  
Archive**

University of Zurich  
University Library  
Strickhofstrasse 39  
CH-8057 Zurich  
[www.zora.uzh.ch](http://www.zora.uzh.ch)

---

Year: 2018

---

## **Morphometric analysis of spread platelets identifies integrin $\alpha$ -specific contractile phenotype**

Lickert, Sebastian ; Sorrentino, Simona ; Studt, Jan-Dirk ; Medalia, Ohad ; Vogel, Viola ; Schoen, Ingmar

**Abstract:** Haemostatic platelet function is intimately linked to cellular mechanics and cytoskeletal morphology. How cytoskeletal reorganizations give rise to a highly contractile phenotype that is necessary for clot contraction remains poorly understood. To elucidate this process in vitro, we developed a morphometric screen to quantify the spatial organization of actin fibres and vinculin adhesion sites in single spread platelets. Platelets from healthy donors predominantly adopted a bipolar morphology on fibrinogen and fibronectin, whereas distinguishable, more isotropic phenotypes on collagen type I or laminin. Specific integrin  $\alpha$  inhibitors induced an isotropic cytoskeletal organization in a dose-dependent manner. The same trend was observed with decreasing matrix stiffness. Circular F-actin arrangements in platelets from a patient with type II Glanzmann thrombasthenia (GT) were consistent with the residual activity of a small number of  $\alpha$  integrins. Cytoskeletal morphologies in vitro thus inform about platelet adhesion receptor identity and functionality, and integrin  $\alpha$  mechanotransduction fundamentally determines the adoption of a bipolar phenotype associated with contraction. Super-resolution microscopy and electron microscopies further confirmed the stress fibre-like contractile actin architecture. For the first time, our assay allows the unbiased and quantitative assessment of platelet morphologies and could help to identify defective platelet behaviour contributing to elusive bleeding phenotypes.

DOI: <https://doi.org/10.1038/s41598-018-23684-w>

Posted at the Zurich Open Repository and Archive, University of Zurich

ZORA URL: <https://doi.org/10.5167/uzh-151290>

Journal Article

Published Version



The following work is licensed under a Creative Commons: Attribution 4.0 International (CC BY 4.0) License.

Originally published at:

Lickert, Sebastian; Sorrentino, Simona; Studt, Jan-Dirk; Medalia, Ohad; Vogel, Viola; Schoen, Ingmar (2018). Morphometric analysis of spread platelets identifies integrin  $\alpha$ -specific contractile phenotype. *Scientific Reports*, 8(1):5428.

DOI: <https://doi.org/10.1038/s41598-018-23684-w>

# SCIENTIFIC REPORTS

OPEN

## Morphometric analysis of spread platelets identifies integrin $\alpha_{IIb}\beta_3$ -specific contractile phenotype

Sebastian Lickert<sup>1</sup>, Simona Sorrentino<sup>2</sup>, Jan-Dirk Studt<sup>3</sup>, Ohad Medalia<sup>2,4</sup>, Viola Vogel<sup>1</sup> & Ingmar Schoen<sup>1,5</sup>

Haemostatic platelet function is intimately linked to cellular mechanics and cytoskeletal morphology. How cytoskeletal reorganizations give rise to a highly contractile phenotype that is necessary for clot contraction remains poorly understood. To elucidate this process *in vitro*, we developed a morphometric screen to quantify the spatial organization of actin fibres and vinculin adhesion sites in single spread platelets. Platelets from healthy donors predominantly adopted a bipolar morphology on fibrinogen and fibronectin, whereas distinguishable, more isotropic phenotypes on collagen type I or laminin. Specific integrin  $\alpha_{IIb}\beta_3$  inhibitors induced an isotropic cytoskeletal organization in a dose-dependent manner. The same trend was observed with decreasing matrix stiffness. Circular F-actin arrangements in platelets from a patient with type II Glanzmann thrombasthenia (GT) were consistent with the residual activity of a small number of  $\alpha_{IIb}\beta_3$  integrins. Cytoskeletal morphologies *in vitro* thus inform about platelet adhesion receptor identity and functionality, and integrin  $\alpha_{IIb}\beta_3$  mechanotransduction fundamentally determines the adoption of a bipolar phenotype associated with contraction. Super-resolution microscopy and electron microscopies further confirmed the stress fibre-like contractile actin architecture. For the first time, our assay allows the unbiased and quantitative assessment of platelet morphologies and could help to identify defective platelet behaviour contributing to elusive bleeding phenotypes.

Mechanical platelet functions during thrombosis comprise primary adhesion at injured vessel walls, secondary aggregation, and clot retraction. Each process involves different adhesion receptors and activation pathways but all three require active actomyosin contractile forces. The biophysical mechanisms by which the engagement of different receptors and associated signalling events determine the cytoskeletal architecture associated with the specific platelet sub-phenotypes for adhesion or aggregation, respectively, remain poorly understood. Integrin  $\alpha_{IIb}\beta_3$ -mediated attachment to fibrinogen (FG) results in high single platelet actomyosin contractile forces in the range of 15–35 nN<sup>1–3</sup>. How platelets achieve a similar contraction efficiency as myoblasts<sup>1</sup> with their highly aligned sarcomeres is unclear. As platelet adhesion and aggregation pose different mechanical requirements, it could be suspected that different cytoskeletal morphologies mediate these different tasks.

The morphology of spreading platelets has been extensively studied *in vitro*. Platelet spreading on glass proceeds fast (1–2 min) and independent of adhesion protein identity<sup>4–6</sup>. Further spreading (3–10 min) on FG or fibronectin (FN) relies on integrin  $\alpha_{IIb}\beta_3$ <sup>4,7</sup>, involves the formation of tight cell-substrate contacts<sup>4</sup> that are enriched with talin<sup>8,9</sup>, vinculin<sup>8–10</sup> and Pdlim7<sup>11</sup>, and requires actin remodeling<sup>9</sup>. Fully spread platelets on FG have parallel, triangular, or circular F-actin bundles<sup>9</sup> that contain myosin, tropomyosin and  $\alpha$ -actinin in patches<sup>8,12</sup>, thereby resembling essential features of contractile stress fibres<sup>13</sup>. F-actin arrangements depend on density<sup>14</sup> and immobilization<sup>15</sup> of FG and are mediated by integrin signalling pathways involving FAK<sup>15</sup>, Src kinase or Rac<sup>14</sup>. Despite this evidence for a role of integrin outside-in signalling for F-actin cytoskeletal organization, several open

<sup>1</sup>Laboratory of Applied Mechanobiology, Department of Health Sciences and Technology, ETH Zurich, Vladimir-Pregel-Weg 4, 8093, Zurich, Switzerland. <sup>2</sup>Department of Biochemistry, University of Zurich, Winterthurerstr. 190, 8057, Zurich, Switzerland. <sup>3</sup>Division of Hematology, University Hospital Zurich, Rämistrasse 100, 8091, Zurich, Switzerland. <sup>4</sup>Department of Life Sciences and the National Institute for Biotechnology in the Negev, Ben-Gurion University, 84105, Beer-Sheva, Israel. <sup>5</sup>Present address: Department of Molecular and Cellular Therapeutics and Irish Centre for Vascular Biology, Royal College of Surgeons in Ireland, 123 St Stephen's Green, Dublin 2, Ireland. Correspondence and requests for materials should be addressed to V.V. (email: [viola.vogel@hest.ethz.ch](mailto:viola.vogel@hest.ethz.ch)) or I.S. (email: [ingmarschoen@rcsi.ie](mailto:ingmarschoen@rcsi.ie))

questions remain. Are these cytoskeletal arrangements specific for integrin  $\alpha_{\text{IIb}}\beta_3$ ? Do they contain common signatures that correlate with integrin signalling or  $\alpha_{\text{IIb}}\beta_3$  mechanosensing<sup>16</sup>? How do variable integrin  $\alpha_{\text{IIb}}\beta_3$  surface expression levels<sup>17</sup> or mutations that are associated with Glanzmann thrombasthenia (GT) affect cytoskeletal organization and the capability to develop a contractile phenotype?

A recent study<sup>3</sup> revealed a potential link between reduced platelet contractility and certain bleeding phenotypes. Since platelet aggregometry tests of these patients were normal, a contractility test could fill a 'blind spot' for testing of biomechanical platelet functions. Inhibition of different platelet adhesion receptors resulted in reduced contractility but also distinctly different cytoskeletal morphologies<sup>18</sup>. We thus hypothesize that microscopy images contain valuable information about platelet contractile functions. Until now, platelet cytoskeletal morphologies have been reported without further statistical evaluation<sup>7–10,12</sup>. A systematic high-content screening of platelet morphology, as routinely performed for drug discovery with other adherent cells<sup>19</sup>, is lacking but necessary to establish robust morphological structure-function relationships. We here use confocal fluorescence microscopy to address this relation under well-defined experimental settings. Spreading of washed platelets *in vitro* on ligand-coated surfaces and weak coagulant conditions (5  $\mu\text{M}$  ADP) were chosen to reduce variability. This setting was specifically designed to interrogate the FG – integrin  $\alpha_{\text{IIb}}\beta_3$  – actomyosin interplay which is essential for platelet aggregation. Advanced image analysis reliably identified platelet subpopulations and revealed the predominance of platelets with highly aligned actin cytoskeleton. This morphological phenotype was exclusively linked to  $\alpha_{\text{IIb}}\beta_3$  integrins, depended on their number, clustering, and outside-in signalling capabilities, and was lost on soft matrices or in platelets from a type II GT patient. Platelet cytoskeletal textures thus might serve as biomarkers for haemostatic or defective thrombus formation.

## Results

**Morphological phenotyping of healthy human platelets on fibrinogen.** We first imaged human platelets with the cell-permeable F-actin stain SiR-actin<sup>20</sup> (Supplementary Movie S1 and Supplementary Fig. S1) to determine a seeding time that yields reproducible cytoskeletal morphologies. When platelets touched the FG-coated surface, filopodia and a faint actin ring at the cell periphery appeared. Filaments moved radially outwards from the actin-rich centre and bundled. This transient remodelling lasted 3–5 minutes and resulted in strong actin bundles lining a central void region. The timescale of actin remodelling agreed well with dynamics of initial single platelet contraction<sup>1</sup> and adhesion site formation<sup>4,21</sup>. The stable final arrangement justified the usage of fixed samples for better image quality and larger statistics.

F-actin (Fig. 1a) and vinculin (Fig. 1b) in fully spread platelets in the presence of ADP showed a wide range of cytoskeletal patterns including bipolar, triangular, star or ring shapes, as reported previously<sup>8,9,12,22</sup>. Despite their variable shape and size, most morphologies were characterized by strong F-actin bundles (Fig. 1a) anchored at pronounced vinculin-containing adhesion sites (Fig. 1b).

To systematically analyse these morphologies, a largely automated single cell analysis was developed (see Supplementary Text and Supplementary Figs S2–S4). Platelets' size and shape, the degree of actin fibre alignment (from isotropic 0, to completely aligned 1) and their radial order (from circumferential 0, to radial +1) were extracted from images of F-actin (Fig. 1c). While the spreading area is a widely accepted measure of platelet size, the other parameters demand further explanation. The ellipticity quantifies the cell elongation that accompanies cytoskeletal polarization in adherent cell types<sup>23,24</sup>. The fibre alignment is a measure for the anisotropy of actin filaments. According to physical models, it arises from the coupling of an anisotropic cell shape with cellular mechanosensing<sup>23</sup>. The radial order was here introduced to distinguish between different isotropic arrangements of the cytoskeleton, namely ring-shaped or star-shaped, that otherwise cannot be distinguished by their (low) fibre alignment parameters. From vinculin images, we quantified the distribution of adhesion sites around the cell by fitting a Fourier series to the circumferential intensity profile (Fig. 1b). The resultant Fourier amplitudes were used to assign a characteristic morphology (isotropic, bipolar, triangular) to the cell (see Methods).

The spreading area of platelets from healthy donors ranged from 10 to 60  $\mu\text{m}^2$ , with a mean at 31  $\mu\text{m}^2$  (Fig. 1d). Platelets with areas larger than 20  $\mu\text{m}^2$  were regarded as fully spread and subjected to further analysis. Despite their rather circular shape (Fig. 1e), most platelets had a strongly polarized F-actin cytoskeleton with a mean fibre alignment of 0.50 (Fig. 1f) which weakly depended on cell elongation (Supplementary Fig. S5). No clear preference for radial or circumferential actin fibres was observed (Fig. 1g). The circumferential distribution of vinculin adhesion sites (Fig. 1b) revealed a predominance of bipolar (II, 65%) over triangular (III, 19%) and isotropic (I, 13%) adhesion morphologies (Fig. 1i). Cytoskeletal order and adhesion site distribution were correlated, with aligned and rather star-shaped F-actin for the bipolar morphology, and more isotropic and ring-like F-actin organization for the triangular and isotropic morphologies (Supplementary Fig. S4c,d). This contour plot can thus be regarded as a valid representation of overall adhesion morphologies in the whole platelet population. A representative cell (Fig. 1j) picked from its maximum exemplifies the predominant adhesion phenotype. We conclude that the predominant cytoskeletal architecture of spread platelets on FG in healthy donors was characterized by highly parallel F-actin fibres associated with peripheral adhesions at both ends.

**Assay validation and physiological variability.** We next assessed the repeatability and reproducibility of platelet adhesion morphologies in the presence of ADP. Independent processing of the same blood sample yielded highly consistent results (Table 1, 'intra'). The morphology was robust with prolonged incubation up to four hours (Supplementary Fig. S6). In the absence of ADP, platelet spreading area, ellipticity, and radial order were unaffected whereas the fibre alignment was slightly decreased (Supplementary Fig. S7). Storage of the blood sample for 24 hours before analysis had a similar effect (Supplementary Fig. S8). We conclude that platelet adhesion morphology was highly reproducible under the chosen assay settings, i.e. in the presence of ADP and within a few hours after blood withdrawal.

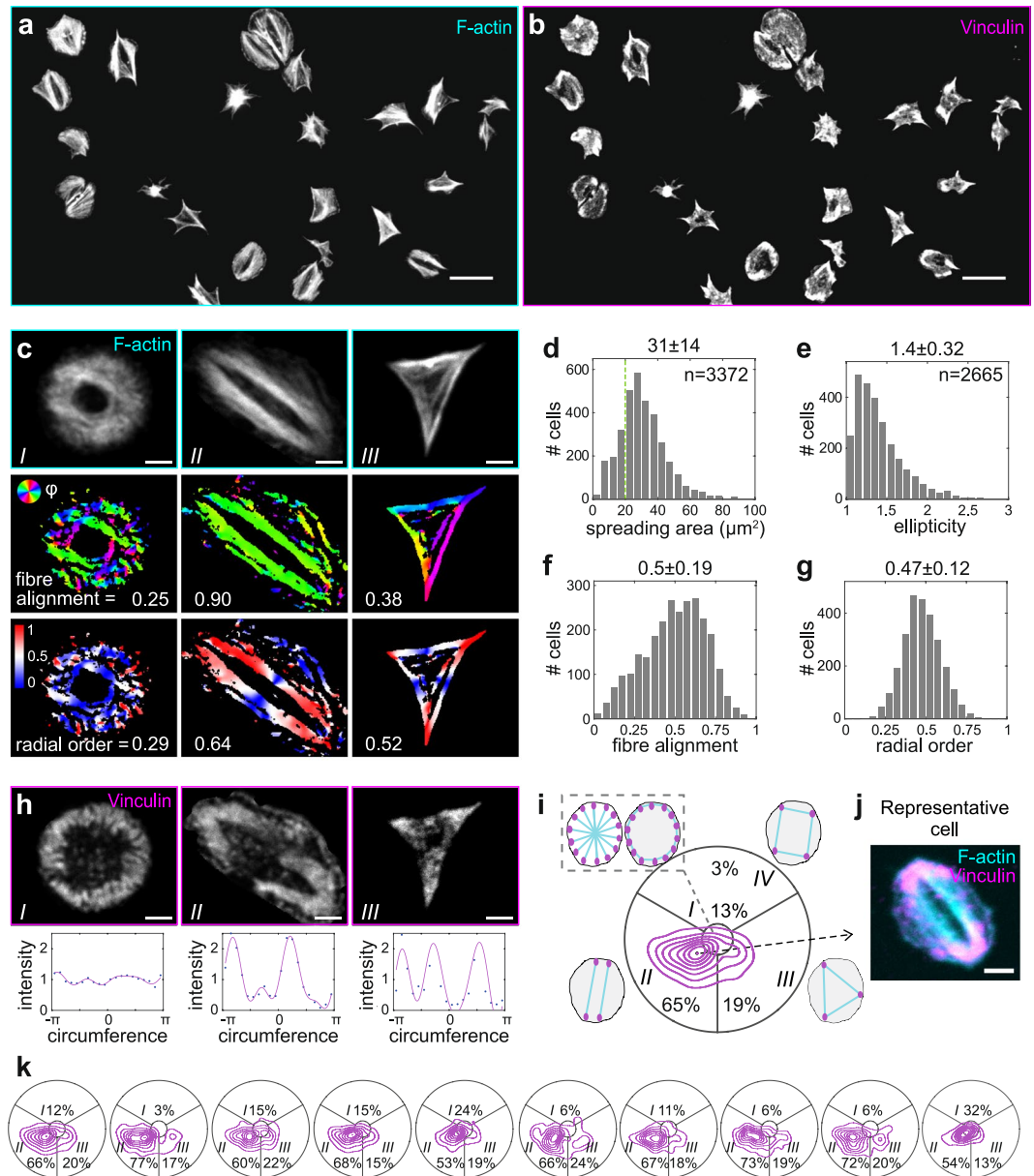


**Figure 1.** Morphometric analysis of the contractile cytoskeleton in spread platelets reveals predominance of a bipolar phenotype. Representative (a) F-actin and (b) vinculin confocal micrographs of platelets from a healthy donor after 60 min of spreading on fibrinogen (FG). (c) Single cell actin cytoskeletal analysis. Top row: examples of distinctive F-actin patterns. Middle row: Orientation of actin fibres (colour-coded) and derived fibre alignment parameter. 1 = perfect alignment, 0 = random. Bottom row: Radial order (colour-coded). 1 = radial (red), 0 = circumferential (blue), 0.5 = mixed (white). (d) Single cell spreading area. Cells larger than  $20\mu\text{m}^2$  (green dotted line) were further analysed in terms of their (e) shape (1: round,  $>1$ : elongated), (f) fibre alignment, and (g) radial order. (h) Spatial distribution of adhesion sites. Top row: vinculin stainings, same cells as in c. Bottom row: projected circumferential vinculin intensity profile (dots). A Fourier fit (magenta solid line) was used to extract the components up to 4th order (bipolar, triangular, and quadratic arrangements). (i) Contour plot of the number of cells with adhesion sites arranged isotropically (middle sector) or in a bipolar (lower left sector), triangular (lower right sector), or quadratic (upper sector) pattern. (j) Representative cell for the predominant morphology picked according to the maximum in the vinculin morphology plot (dot in i). Data were pooled from 10 healthy donors with 200–400 platelets per donor. (k) Comparison of donor-to-donor variability by vinculin morphology (cf. also Supplementary Fig. S9). Donors comprised 7 males and 3 females with a median age of 31.5 years (range 27–44 years). Scale bars:  $10\mu\text{m}$  (a,b),  $2\mu\text{m}$  (c,h,j). A comprehensive description of the image analysis is given in the Supplementary Text and Supplementary Figs S2–S4.

To test the physiological variability of platelets from the same donor, withdrawals were repeated at intervals of more than one week. Resulting CVs were only slightly higher (Table 1, ‘in-donor’) than the assay reproducibility. When assessing variation between donors, the contour plots consistently showed primary bipolar and secondary

	Area/ $\mu\text{m}^2$	Ellipticity	Fibre alignment	Radial order	CC <sup>morph</sup>
intra	1.30 (0.04)	0.039 (0.10)	0.022 (0.04)	0.007 (0.01)	0.91 (0.02)
in-donor	3.68 (0.12)	0.104 (0.25)	0.016 (0.03)	0.050 (0.10)	0.91 (0.02)
inter-donor	3.62 (0.12)	0.064 (0.16)	0.069 (0.14)	0.046 (0.09)	0.83 (0.10)

**Table 1.** Assay validation and physiological variability. Given are the mean differences in absolute values or the respective coefficients of variation (CV, in brackets) of morphometrics between different samples for spreading area, ellipticity, fibre alignment, and radial order. The similarity between vinculin morphology plots was quantified by a normalized cross-correlation ('CC<sup>morph</sup>'). Intra: four independently processed samples from the same blood probe. In-donor: two samples each from repeated withdrawals from the same donor, n = 4 donors in total. Inter-donors: samples from n = 10 different donors.

triangular subpopulations (Fig. 1k). Statistically significant differences between donors were detected in few cases (Supplementary Fig. S9), and CVs were of similar magnitude (Table 1, 'inter-donor') as for repeated withdrawals. In conclusion, actin and vinculin morphometrics were more sensitive than spreading area and shape, morphological signatures were donor-specific, yet the bipolar morphologies and strong fibre alignment dominated in all healthy individuals.

**Specificity of the bipolar morphology for ligands of integrin  $\alpha_{\text{IIb}}\beta_3$ .** To test whether the morphology *in vitro* correlates with the engagement of specific adhesion receptors, we seeded platelets on surfaces coated with FG, fibronectin (FN), laminin (LN), or collagen type 1 (COL1). FG and FN are bound primarily by integrin  $\alpha_{\text{IIb}}\beta_3$  in the context of platelet aggregation, whereas COL1 is recognized by integrin  $\alpha_2\beta_1$  (and GPVI) and LN by integrin  $\alpha_6\beta_1$  in the context of platelet adhesion to the sub-endothelium<sup>25</sup>. Platelets adhered to all surfaces (Fig. 2a). The bipolar phenotype dominated on FG and FN, whereas most platelets on LN and COL1 showed isotropic or disordered adhesion patterns (Fig. 2b). Spreading areas on FG, FN, and LN were comparable (mean  $30\mu\text{m}^2$ ) but smaller on COL1 (mean  $20\mu\text{m}^2$ ; Fig. 2d). Platelet shape was similar on FG, FN, and COL1 but rounder on LN (Supplementary Fig. S10a). The F-actin cytoskeleton was strongly aligned on FG and FN (mean > 0.5) but strikingly less on LN (mean 0.4) and COL1 (mean 0.35; Fig. 2e). On LN, it was arranged in a pronounced circumferential ring<sup>26,27</sup> (Fig. 2a,b) as reflected by the lower radial order (mean 0.35; Supplementary Fig. S10b). The spatial distribution of vinculin adhesion sites on FG and FN was similar but substantially different on COL1 and LN (Fig. 2f). Similar results were obtained when stimulating the platelets with 0.05 or 0.1 U/mL thrombin instead of ADP, with a slightly enhanced fibre alignment on FG and FN (Supplementary Fig. S11). In summary, platelets developed the same morphologies on FN and FG, but highly discriminable phenotypes on other adhesion proteins.

To determine the contribution of integrin  $\alpha_{\text{IIb}}\beta_3$  to morphologies on different adhesion proteins, we applied the specific inhibitor RUC-4<sup>28</sup> at saturating concentration (100  $\mu\text{M}$ ). The presence of RUC-4 effectively abolished platelet spreading on FG and FN, whereas on LN or COL1 it had no significant effect on platelet morphologies (Fig. 2c–f). We conclude that the bipolar phenotype is exclusively associated with adhesion ligands that play a role in platelet aggregation and it requires integrin  $\alpha_{\text{IIb}}\beta_3$ .

**Sensitivity of the bipolar morphology to integrin  $\alpha_{\text{IIb}}\beta_3$  outside-in signalling.** Integrin  $\alpha_{\text{IIb}}\beta_3$  is expressed at ~80'000 copies per platelet<sup>29,30</sup>, yet the functional importance of this high copy number and its variations remain unclear. To distinguish between the effects of binding strength, clustering and outside-in signalling on platelet morphology, three different approaches were chosen to perturb the number of engaged  $\alpha_{\text{IIb}}\beta_3$  integrins.

First, we performed a dose-response experiment with RUC-4 that blocks access to the binding pocket of integrin  $\alpha_{\text{IIb}}\beta_3$  but does not 'prime' it for outside-in signalling<sup>28,31–33</sup> (Fig. 3a,i). F-actin became gradually less aligned (IC<sub>50</sub> 1.3  $\mu\text{M}$ , Fig. 3a,iii) with increasing RUC-4 concentrations before the spreading area was affected (IC<sub>50</sub> 6.3  $\mu\text{M}$ , Fig. 3a,ii). Concomitantly, the population shifted from the bipolar to a more isotropic phenotype (Fig. 3a,iv). The DMSO control was negative (Supplementary Fig. S12). Hence, a high number of functional  $\alpha_{\text{IIb}}\beta_3$  integrins was needed for the bipolar phenotype.

Second, we used the  $\alpha_{\text{IIb}}\beta_3$  antagonist eptifibatide (Integrilin) that causes ligand-induced conformational changes related to outside-in signalling<sup>34</sup> similar to natural ligands like FG<sup>35</sup> (Fig. 3b,i). F-actin alignment decreased abruptly (IC<sub>50</sub> 17  $\mu\text{M}$ , Fig. 4b,iii) and the bipolar phenotype disappeared (Fig. 3b,iv) shortly before spreading was inhibited (IC<sub>50</sub> 31  $\mu\text{M}$ , Fig. 3b,ii). The about 5–7 fold steeper dose-response curves compared with RUC-4 indicate that eptifibatide-induced outside-in signalling might partially compensate for the reduced number of engaged integrins.

Third, we varied the density of surface-immobilized FG (Supplementary Fig. S13) which affects integrin clustering, early adhesion stabilization, integrin signalling and platelet spreading<sup>14</sup> (Fig. 3c,i). Unspecific surface interactions were blocked by a backfill with the non-fouling agent PAcrAm-g-PMOXA<sup>36,37</sup> (Supplementary Fig. S14). The morphology of platelets changed gradually with decreasing FG surface density. A pronounced ring-like F-actin and vinculin arrangement prevailed at intermediate densities (around 0.2  $\mu\text{g}/\text{mL}$ , Fig. 3c,iv) which was accompanied by reduced actin alignment (Fig. 3c,iii) and a loss of the bipolar signature (Fig. 3c,iv). Spreading was suppressed below 0.1  $\mu\text{g}/\text{mL}$  (EC<sub>50</sub> 0.08  $\mu\text{g}/\text{mL}$ , Fig. 3c,ii). We conclude that clustering of integrin  $\alpha_{\text{IIb}}\beta_3$  sensitively affected the cytoskeletal organization and was required for the bipolar phenotype.



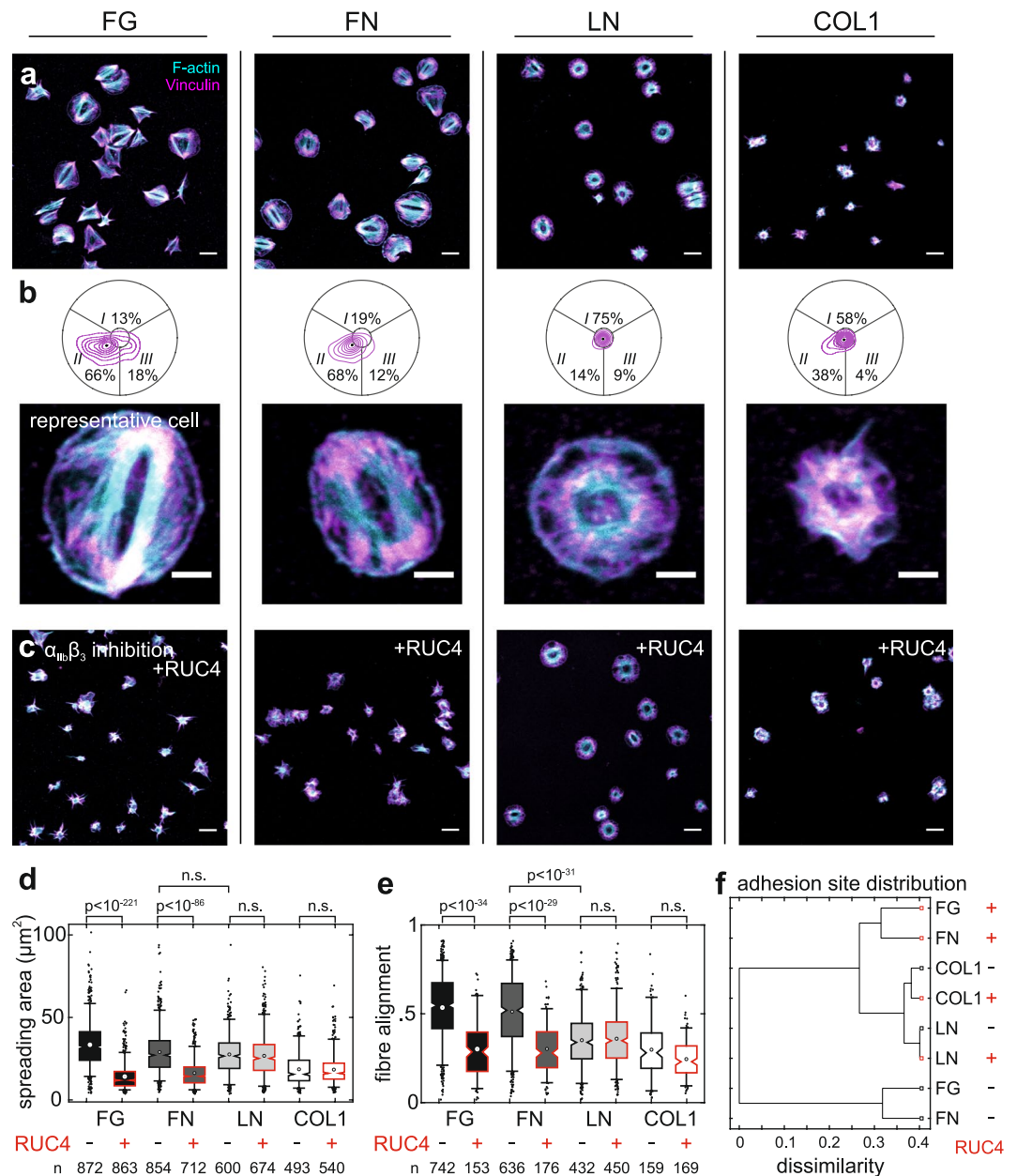


**Figure 2.** The bipolar phenotype is exclusively observed on ligands of integrin  $\alpha_{IIb}\beta_3$ . **(a)** Overview of healthy platelets after 60 min of spreading on the ligands fibrinogen (FG), fibronectin (FN), laminin (LN) and collagen type I (COL1). Cyan: F-actin; magenta: vinculin. **(b)** Spatial distribution of vinculin adhesion sites in platelets and representative cells. **(c)** Spread platelets in the presence of 100  $\mu\text{M}$  of the  $\alpha_{IIb}\beta_3$ -specific inhibitor RUC-4. Quantitative F-actin analysis for **(d)** the spreading area and **(e)** the fibre alignment is shown for each ligand with and without blocking of  $\alpha_{IIb}\beta_3$  integrins (cf. also Supplementary Fig. S10). **(f)** Classification according to the similarity between vinculin adhesion site distributions. The classification tree clearly shows that morphologies on FG and FN are very similar and heavily affected by inhibiting  $\alpha_{IIb}\beta_3$  whereas COL1 and LN are very different from this morphology and from each other and not affected by RUC-4. Data were pooled from three healthy male donors (33–44 years). Scale bars: 10  $\mu\text{m}$  (a,c), 2  $\mu\text{m}$  (b).

In summary, these perturbations of integrin  $\alpha_{IIb}\beta_3$  reveal an important role of functional integrin outside-in signalling and clustering for the bipolar morphology.

**Dependency of the bipolar morphology on mechanosensing through integrin  $\alpha_{IIb}\beta_3$ .** Matrix stiffness modulates the assembly and remodeling of integrin junctions<sup>38–40</sup> and affects cell spreading<sup>41</sup>, cytoskeletal organization<sup>23</sup>, traction forces<sup>38,41</sup>, and platelet activation<sup>42</sup>. To study the effect of integrin  $\alpha_{IIb}\beta_3$  mechanosensing on cytoskeletal morphology, platelets were seeded on FG-coated polyacrylamide hydrogels with a stiffness between 2–35 kPa (Fig. 4a). Platelets spread on all but the softest gel (Fig. 4b,c), in agreement with previous

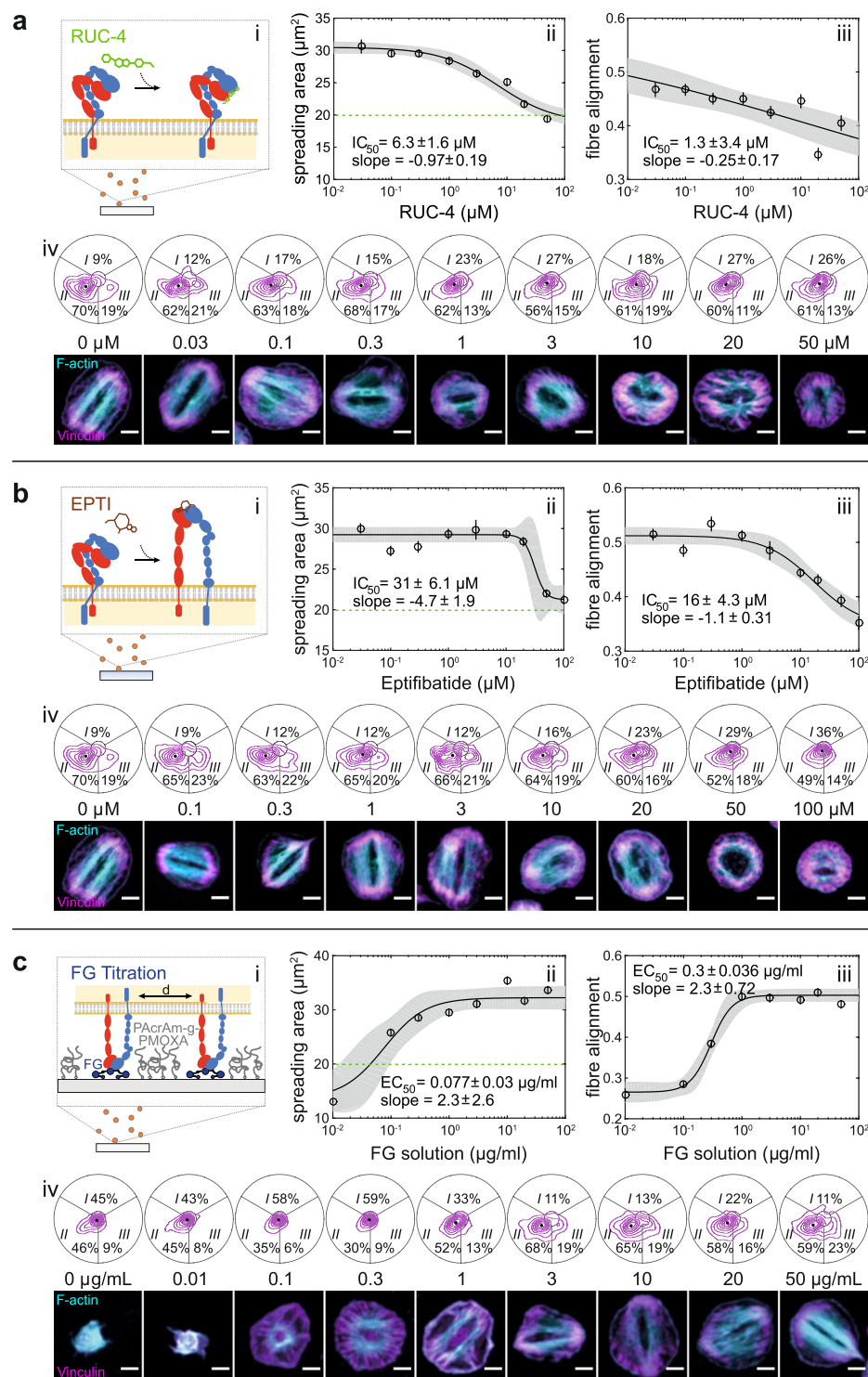


**Figure 3.** The bipolar morphology depends on integrin  $\alpha_{IIb}\beta_3$  outside-in signalling. **(a)** Titration series with the non-priming inhibitor RUC-4 that blocks FG binding of  $\alpha_{IIb}\beta_3$ , **(b)** Titration series with Eptifibatide which induces conformational changes in  $\alpha_{IIb}\beta_3$  related to outside-in signalling. **(c)** Dilution series of surface-immobilized FG that affects integrin clustering (cf. also Supplementary Figs S13 and S14). Shown are **(i)** schematic representations, dose-response curves for **(ii)** spreading area and **(iii)** fibre alignment, and **(iv)** contour plots of the spatial distribution of adhesion sites together with representative cells. Solid lines and grey regions are fits to a logistic Hill equation and their 95% confidence intervals, respectively. Data pooled from three male donors (33–44 years) each. Platelets were preincubated for 10 minutes with inhibitors and seeded for 60 minutes in their presence. Scale bars: 2  $\mu m$ .

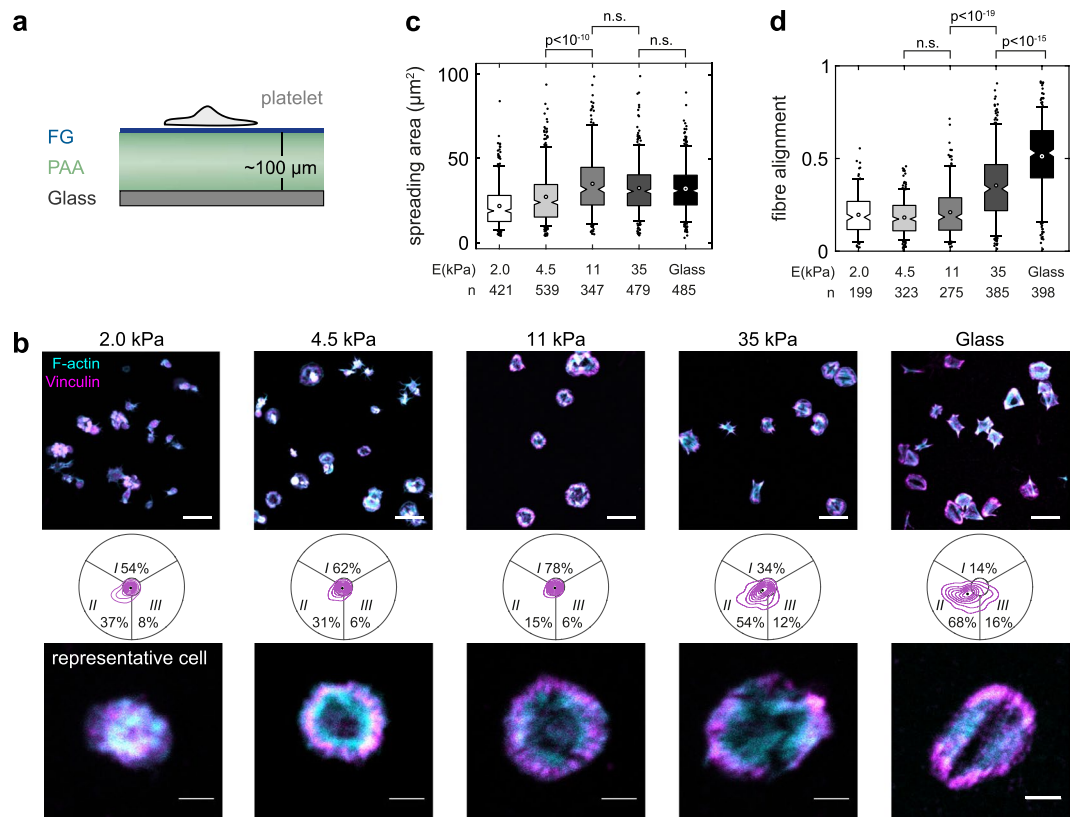


**Figure 4.** The bipolar morphology is mechanosensitive. (a) Platelets were seeded for 60 min on FG that was covalently crosslinked on polyacrylamide (PAA) hydrogels of different stiffness. Schematic not to scale. (b) Overview images (top), adhesion morphology plots (middle) and representative cells (bottom) of platelets on 2.0 kPa, 4.5 kPa, 11 kPa, 35 kPa gels and on glass. Scale bars: 10  $\mu$ m (overview), 2  $\mu$ m (representative cells). (c) Cells spread on gels above 4.5 kPa. (d) Actin fibre alignment increased above 11 kPa. Data were pooled from one male and two female donors (28–54 years). See also Supplementary Fig. S15.

findings<sup>42</sup>. Like on glass, most platelets on the hardest gel showed a bipolar signature (Fig. 4b) and an aligned actin cytoskeleton (Fig. 4d). Below 11 kPa, the bipolar phenotype was gradually lost and actin organization became more isotropic (Fig. 4b,d). These morphological features resembled those for intermediate RUC-4 concentrations (cf. Fig. 3a) or reduced FG density (cf. Fig. 3c). Please note that the FG density was similar on all gels<sup>43</sup> (Supplementary Fig. S15). We conclude that an extracellular mechanical resistance to traction forces through integrin  $\alpha_{IIb}\beta_3$  is needed to achieve a strong alignment of the cytoskeleton.

**Ultrastructure of the healthy cytoskeletal morphology on fibrinogen.** Although electron and super-resolution microscopes are not yet well suited for studying a large number of platelets in a statistical manner, they here were used to further substantiate our conclusions derived from confocal microscopy. Most microfilaments in SEM images ran in parallel from one side of the cell to the other and fused in-between into larger bundles (Fig. 5a, inset, arrowheads), as previously reported<sup>44,45</sup>. Direct stochastic optical reconstruction microscopy (dSTORM)<sup>46</sup> of F-actin revealed densely arranged and strongly aligned actin filaments within bundles (Fig. 5b and Supplementary Fig. S16a), whereas F-actin in the cell periphery formed a dendritic network (Fig. 5b, inset) as also obvious from cryo-electron tomograms (cryo-ET; Supplementary Fig. S17a). The good agreement between SEM with cryo-ET images and F-actin dSTORM images indicates that the majority of filamentous structures in SEM images were actin microfilaments.

We further investigated the composition of actin bundles and their respective adhesion sites. Dual-colour dSTORM images showed string-like vinculin stainings along the ends of actin fibres (Fig. 5c and Supplementary Fig. S16b) similar to observations in focal adhesions of fibroblasts<sup>47</sup>. The motor protein myosin IIA co-localized with actin bundles (Fig. 5d, red) and was phosphorylated at its light chain (Supplementary Fig. S18), confirming that F-actin bundles were contractile. The actin-binding protein  $\alpha$ -actinin was localized in adhesion sites and lesser in actin bundles (Fig. 5d, green). Our inability to detect an alternating arrangement of these two latter proteins along F-actin bundles (Fig. 5d, inset; in contrast to a previous report<sup>12</sup>) or bipolar myosin mini-filaments as two hallmark features of stress fibres<sup>13,48,49</sup> might be partially owed to the poor immunolabeling efficiency for myosin and  $\alpha$ -actinin.

As the marginal band dominates the passive mechanical properties of resting platelets<sup>50</sup>, we visualized microtubules by 3D dSTORM (Fig. 5e and Supplementary Fig. S16c). In agreement with previous observations<sup>51,52</sup>, microtubules in fully spread platelets on FG mostly formed uncurled, spaghetti-nest like structures, with few



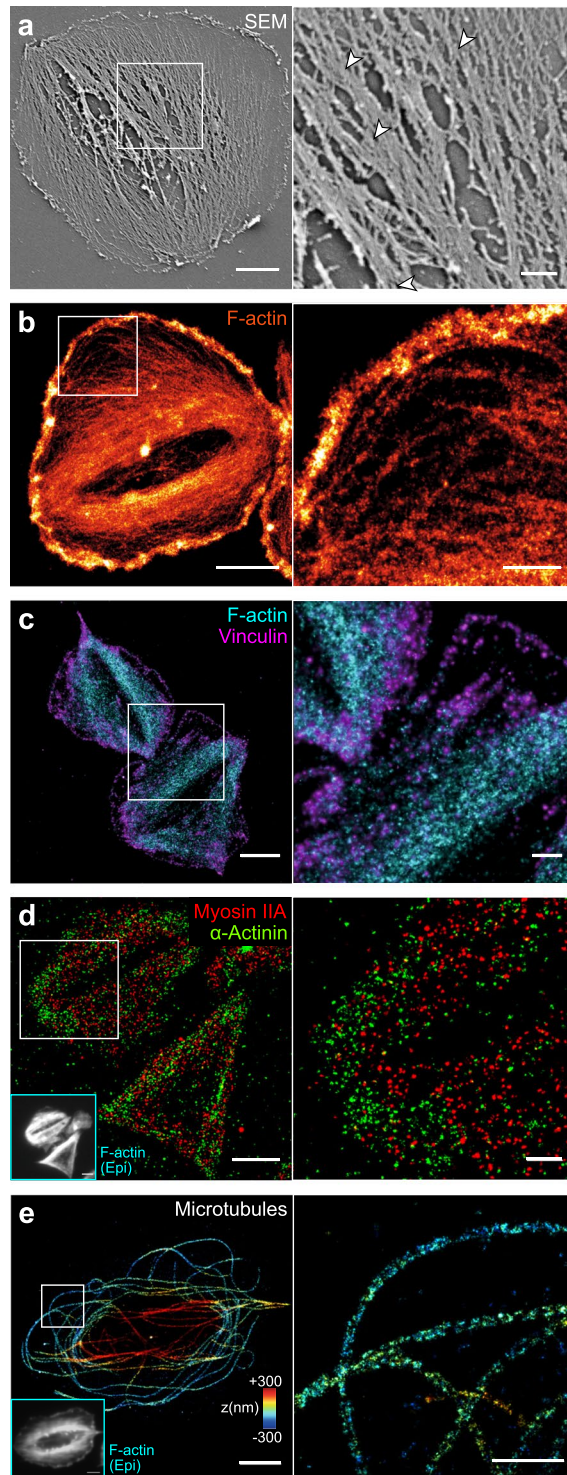


**Figure 5.** Electron microscopy and superresolution (dSTORM) imaging of the cytoskeletal morphology of healthy human platelets. Platelets were seeded for 60 min on FG on glass, then detergent extracted and fixed. Shown are representative cells (left) and a magnified inset (right). **(a)** Scanning electron microscopy (SEM) image. **(b)** dSTORM image of F-actin. **(c)** Dual-colour dSTORM image of vinculin (magenta) and F-actin (cyan). **(d)** Dual-colour dSTORM image of myosin IIA (red) and  $\alpha$ -actinin (green). Inset: epifluorescence image of F-actin in the same cells. **(e)** 3D dSTORM image of microtubules. The z-position is colour-coded from blue (basal) to red (apical). Individual microtubules are characterized by the rail-track-like projection of their immunolabelled outer shell. Inset: epi fluorescence image of F-actin in the same cell. Scale bars: 2  $\mu$ m (left column), 500 nm (insets). See also Supplementary Fig. S16 for overview dSTORM images and Supplementary Fig. S17 for cryo-electron tomograms.

remnants of the marginal band. Some microtubules bridged the granulomere at the apical side, whereas others extended into the lamellipodial region (Fig. 5e, inset). Overall, no clear association of microtubules with actin bundles was apparent.

Taken together, the ultrastructure of human platelets confirms that their active mechanical properties are dominated by F-actin microfilaments which are bundled into largely parallel stress fibre-like structures.

**Change of platelet phenotype in Glanzmann thrombasthenia.** Certain mutations in integrin  $\alpha_{IIb}\beta_3$  cause GT, a rare bleeding disorder of autosomal-recessive inheritance accompanied by defective aggregation and clot retraction<sup>53</sup>. To investigate a possible impact on platelet morphology, we recruited a 54-year old female patient with well characterized GT: light transmission aggregometry in platelet-rich plasma demonstrated an impaired platelet aggregation with all agonists (arachidonic acid, thromboxane receptor agonist U46619, ADP, collagen, epinephrine) except ristocetin. Flow cytometry showed significantly reduced (6–7% of normal) surface expression levels of both  $\alpha_{IIb}$  and  $\beta_3$ . The ITGB3 gene carried a heterozygote small duplication in exon 10 (p.Asn470Ter) and a heterozygote missense-mutation in exon 11 (p.Gly605Asp). The duplication is expected to result in severely reduced integrin  $\beta_3$  levels due to pre-mature termination of protein expression. The second mutation affects the same residue as two other described mutations<sup>54,55</sup> which were associated with an abnormal reduction of surface expressed  $\alpha_{IIb}\beta_3$  and its constitutive activation (Supplementary Fig. S19).

Platelets from this GT patient spread on FG in the presence of ADP (Fig. 6a). After 60 minutes, the number of adherent platelets was reduced compared to healthy ( $25 \pm 11$  vs.  $35 \pm 11$  cells per FOV), they were slightly smaller in size (mean  $26 \mu\text{m}^2$ ) but significantly rounder in shape (Supplementary Fig. S20b) and showed pronounced concentric F-actin and vinculin stainings (Fig. 6a,c). Consequently, actin fibre alignment (mean 0.26) and radial order (mean 0.29) were significantly reduced (Fig. 6b) and 82% of platelets had an isotropic phenotype (Fig. 6c). Spreading was completely abolished by RUC-4 (Supplementary Fig. S20) which proves its dependence on  $\alpha_{IIb}\beta_3$ . Results were highly reproducible between separate withdrawals (Supplementary Fig. S21).

SEM images (Fig. 6d) and dSTORM images of F-actin (Fig. 6e and Supplementary Fig. S22a) showed circumferential actin fibres lining the central granulomere but no observable bundling. The dendritic actin network in the lamellipodium was normal (Fig. 6e and Supplementary Fig. S17b). Vinculin adhesion sites were located just outside the F-actin ring (Fig. 6f) with distinct string-like arrangements in the radial direction (Fig. 6f, inset, and Supplementary Fig. S22b). The actin ring zone was positive for pMLC (Supplementary Fig. S23) and thus presumably contractile. Frequent remnants of the microtubule marginal band (Supplementary Fig. S24), reduced spreading in the absence of ADP (Supplementary Fig. S21), and an increased cytoskeletal alignment after prolonged incubation (Supplementary Fig. S25) hint towards an incomplete activation. We conclude that platelets from this GT patient were not able to assemble and stabilize their cytoskeleton towards the healthy bipolar phenotype.

## Discussion

Since reproducibility in the data analysis of cells poses a severe challenge, we introduce an easy-to-implement screening assay for assessing platelet cytoskeletal morphology. It is based on dual-channel (immuno)fluorescence confocal images (Fig. 1) plus automated image analysis (Supplementary Figs S2–S4) and yields highly reproducible metrics (Table 1). In contrast to more complex high-content screening approaches<sup>19</sup>, the measured parameters reflect features that are directly related to mechanical cell function<sup>23</sup> and can be visually verified. We found that cytoskeletal morphometric parameters had a higher reproducibility than spreading area or shape (see CV values, Table 1), distinguished better between different ligands (see FG versus LN in Fig. 2), and were more sensitive to perturbations of integrin  $\alpha_{IIb}\beta_3$  by inhibitors (Fig. 3) or in the GT patient (Fig. 6). They thus could be better or distinct indicators of platelet functionality than spreading area which relies more on actin polymerization rather than on contractility. The visual representation of a heterogeneous population of platelet morphologies by a single plot (Fig. 1i) and the automated selection of a representative cell (Fig. 1j) are further advantages of our method that facilitate the unbiased reporting and comparison of platelet morphologies.

Engagement of the platelet integrin  $\alpha_{IIb}\beta_3$  was necessary for a predominant bipolar organization as shown by ligand selectivity (Fig. 2) and specific blocking (Figs 2c,d, 3a,b). Its disappearance at sub-saturating concentrations of RUC-4 (Fig. 3a), at reduced FG surface densities (Fig. 3c), or in platelets from a GT patient with reduced  $\alpha_{IIb}\beta_3$  surface expression levels (Fig. 6) show that a small number of engaged integrins was insufficient to induce cytoskeletal polarization. The late onset of cytoskeletal changes with the ‘priming’ ligand eptifibatide at around  $3 \mu\text{M}$  (~95% receptor occupancy<sup>56</sup>; Fig. 3b) implies that strong  $\alpha_{IIb}\beta_3$  outside-in signalling could compensate for small numbers of bound integrins and therefore promote the bipolar phenotype. This view is supported by the finding that low ( $3 \mu\text{g/mL}$ ) FG densities alter Src, Rho, and Rac signalling<sup>14</sup> downstream of  $\alpha_{IIb}\beta_3$ . Selective inhibitors against these pathways caused F-actin morphological changes<sup>14</sup> that resemble the isotropic phenotype seen with integrin inhibitors (Fig. 3a,b)<sup>21</sup>, on low FG densities (Fig. 3c), or on soft hydrogels (Fig. 4b). The higher cytoskeletal ordering in platelets on stiffer matrices (Fig. 4d) agrees with mechanosensing mechanisms described for mesenchymal cells, including stem cells<sup>23</sup>, which rely on integrin mechanotransduction, adhesion maturation, and increased traction forces<sup>39,40</sup>. Mechanosensing through  $\alpha_{IIb}\beta_3$  thus simultaneously controls the number of engaged and signalling integrins and thereby dictates cytoskeletal morphology. In summary, the bipolar signature can be seen as a ‘morphological fingerprint’ of functional integrin  $\alpha_{IIb}\beta_3$  outside-in signalling.

Our results have implications for how platelets pull on their environment. The parallel organization of actomyosin filaments in the bipolar phenotype on FG (Figs 1 and 5) enables an efficient force generation and transduction, without the need for an elongated cell shape as in stem cells<sup>23,57</sup> and sarcomere-like ordering as in cardiomyocytes<sup>58,59</sup>, and supports high single platelet forces<sup>1–3</sup>. This cytoskeletal polarization is expected to result in anisotropic (dipolar) tractions<sup>21</sup>. The rather isotropic force fields measured by traction force microscopy (TFM) of platelets on soft hydrogels<sup>2</sup> might be explained by the limited spatial resolution (~1–2  $\mu\text{m}$ ) of TFM and reduced cytoskeletal polarization (Fig. 4D) and contractility<sup>42,60</sup> at 4.5 kPa. The fact that the bipolar phenotype

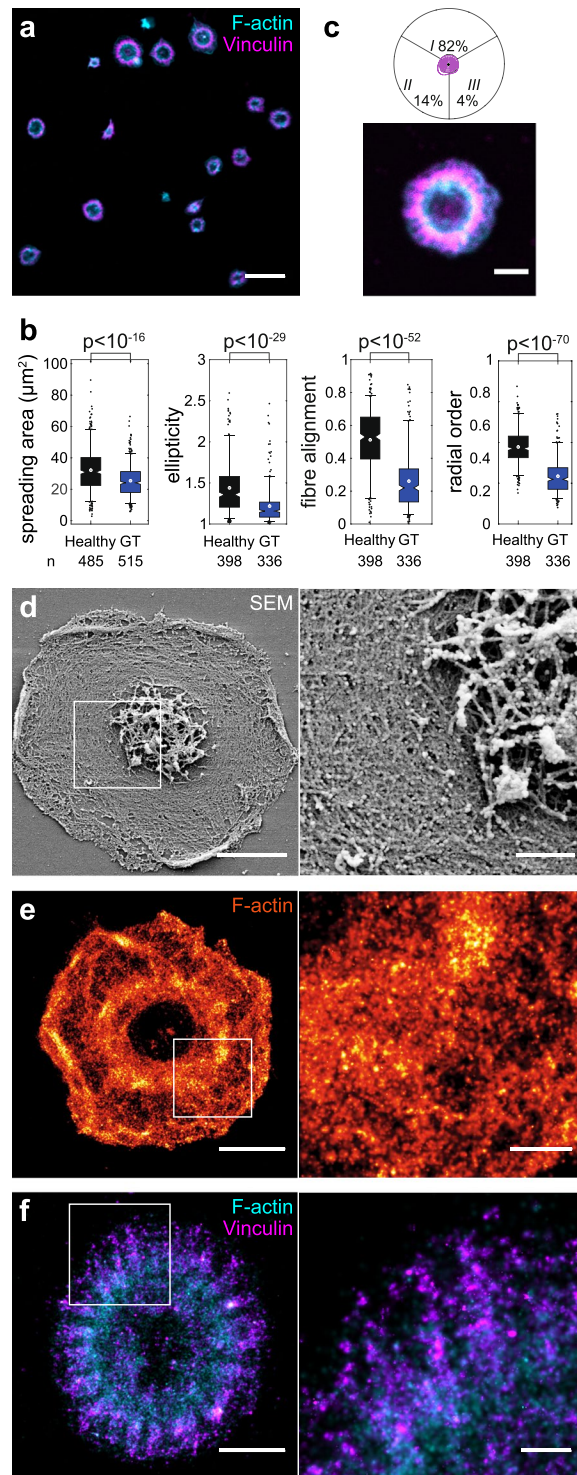


**Figure 6.** Cytoskeletal morphology on FG is altered in platelets from a patient with GT. **(a)** Overview confocal micrograph with F-actin (cyan) and vinculin (magenta). **(b)** Comparison of healthy and GT platelet morphology with respect to spreading area, ellipticity, fibre alignment, and radial order (cf. also Supplementary Figs S20, S21, S25). **(c)** Adhesion sites geometry and representative cell. **(d)** Representative SEM image of detergent extracted GT platelet. **(e)** dSTORM image of F-actin. **(f)** Dual-colour dSTORM image of vinculin (magenta) and F-actin (cyan). Scale bars: 10  $\mu\text{m}$  (a), 2  $\mu\text{m}$  (b and d–f, left column), 500 nm (d–f, insets). See also Supplementary Figs S22 and S24 for overview dSTORM images and S17b for cryo-electron tomograms.

was exclusively observed on FG and FN, but not on COL1 or LN (Fig. 2), suggests that the platelets' capability to polarize their cytoskeleton might especially be relevant in the context of platelet aggregation, aiding efficient clot



retraction. More experiments on the level of single platelets are needed to strengthen the link between cytoskeletal organization and contractility as in other non-muscle cells<sup>61</sup>.

In conclusion, this study demonstrates the first direct morphometric high-content screening of platelets and the identification of subpopulations that differ in their capacity to undergo integrin  $\alpha_{IIb}\beta_3$  mechanotransduction. The tight correspondence of platelet cytoskeletal morphology with a mild GT bleeding phenotype (Fig. 6) and with the action of aggregation antagonists (Fig. 3) suggests that a morphological investigation of platelets might help to determine residual  $\alpha_{IIb}\beta_3$  activity and to diagnose aggregation-related defects. To test this hypothesis, further clinical studies are needed with larger patient numbers. In the future, combining morphometric analysis with automated super-resolution microscopy could enable statistical analysis of platelet ultrastructure.

## Methods

More details on experimental methods and image analysis are available in the Supplementary Information.

**Reagents.** Reagents were purchased from Sigma Aldrich, if not mentioned otherwise. Acid citrate dextrose (ACD) tubes (Sol. B, Vacutainer®, BD, Switzerland); coverslips (18 mm diameter, thickness 1.5; Hecht-Assistent, Germany); human fibrinogen (FG; F3879); human fibronectin (FN; purified from plasma as described previously<sup>62</sup>); rat collagen type I (COL1; 354236, Corning, USA); murine laminin (LN; L2020); poly(acryl-amide)-g-(PMOXA, 1,6-hexanediamine, 3-aminopropyltrimethylsilanol) (7000:4425:116.2:161.3 Mr; 0.2:0.4:0.4 d) (PAcrAm-g-PMOXA) and Poly(L-lysine)-graft-(poly(ethylene glycol)) (20'000:2000 Mr; 0.29 d) (PLL-g-PEG; gift from SuSoS AG, Switzerland); bovine serum albumin (BSA; 05470); Adenosine 5'-diphosphate sodium salt (ADP; A2754); thrombin from human plasma (T4393); eptifibatide (Integrilin; GlaxoSmithKline AG, U.K.); RUC-4 (gift from Prof. B.S. Coller, New York University); SiR-actin kit (CY-SC001, Spirochrome, Switzerland); monoclonal mouse anti-vinculin (V9131); monoclonal mouse anti- $\alpha$ -actinin (A5044); polyclonal rabbit anti-myosin IIa (3403, Cell Signalling Technology, USA); rabbit anti-phospho-myosin light chain 2 (3671 S, Cell Signalling Technology, USA); goat anti-mouse Alexa Fluor 555 (A21424, ThermoFisher, USA); unconjugated donkey anti-mouse or anti-rabbit IgG (Jackson ImmunoResearch, USA); Alexa Fluor 647 NHS ester (A37573, ThermoFisher, USA); CF680 NHS ester (92139, Biotium, USA); Alexa Fluor 488 Phalloidin (A12379, ThermoFisher, USA); Alexa Fluor 647 Phalloidin (A22287, ThermoFisher, USA); ProLong Gold Antifade Mountant (ThermoFisher, USA); (3-Aminopropyl)triethoxysilane (APTES; A3648); ammonium persulfate (APS; 215589); tetramethylethylenediamine (TEMED; T7024); NHS-diazirine (26167, Thermo Fisher, USA).

**Sample preparation.** A comprehensive description of platelet isolation and seeding, fabrication and optimization of the hydrogels substrates, and sample preparation for fluorescence microscopy is found in the Supplementary information. In short, coverslips were coated with FG (50 µg/mL in PBS), FN, LN or COL1 for 1 h at room temperature (RT). For surface ligand titration, the FG bulk concentration was varied and the surface was subsequently blocked by PAcrAm-g-PMOXA (100 µg/mL in PBS, 1 h). Hydrogel substrates were prepared according to literature<sup>63</sup> and covalently coated with FG. Ethical approval was obtained from the Kantonale Ethikkommission Zurich (KEK-ZH-Nr. 2012-0111 and KEK-ZH-Nr. 2013-0027) prior to the commencement of the study. All experiments were performed in accordance with relevant guidelines and regulations. Informed consent was obtained from all participants. Whole blood from healthy adult volunteers or from the GT patient was collected in ACD tubes. Isolated washed platelets were resuspended in Tyrode's buffer (TB) containing 1 mM  $\text{Ca}^{2+}$  and 5 µM ADP, and, where appropriate, eptifibatide or RUC-4. After seeding on coverslips for 1 h at 37 °C, platelets were rinsed once with TB, detergent extracted with 0.25% (v/v) Triton X-100 and 3% (w/v) formaldehyde (FA) in cytoskeleton buffer (CB) for 90 seconds, and subsequently fixed with 3% (w/v) FA in CB for 15 minutes. After three rinses with PBS, samples were stored at 4 °C.

**Microscopy.** Briefly, (immuno)fluorescence stainings for confocal microscopy followed standard procedures (see Supplementary information) and were adapted for dSTORM. Mounted samples were imaged on a Leica SP5 laser scanning confocal microscope (Leica Microsystems, Germany) using a 63× oil immersion objective and excitation at 488 nm and 561 nm, and 16-bit digitization. A pixel size of 60 nm (resulting in a field of view of 123 × 123 µm) and 6× line averaging was used. For statistical analysis of platelet morphology, between 200–250 cells were imaged at 6–10 different positions on the sample. dSTORM imaging was carried out on a home-built setup as described previously<sup>62</sup>. Fitting and analysis of dSTORM movies was performed using the software package SMAP (courtesy of Dr. Jonas Ries, EMBL Heidelberg). For electron microscopy and cryo-EM, please refer to the Supplementary information.

**Image analysis.** A detailed description of the image analysis is given in the Supplementary information. MATLAB code, an example data set and a user guide are provided as Supplementary material that accompanies the online version of this article.

All fluorescence images were denoised by a 3 × 3 median filter and their dynamic range was normalized to the interval [0,1]. For determining cell outlines (Supplementary Fig. S2, step 1 to 2), the background intensity  $bg$  of F-actin images and its standard deviation  $sd$  were determined from the lowest peak in the intensity histogram. F-actin images were then binarized using a threshold of  $bg + 10 \cdot sd$ . Bridges between touching objects were removed by shrinking using an image opening operation with a disk of radius 5 pixels. Objects smaller than 3.6 µm<sup>2</sup> (1000 pixels) were removed and the shrinking of remaining objects was undone. Holes smaller than 1000 pixels were filled and object outlines were smoothed by a 7 × 7 median filter. These automatically generated masks were manually checked and objects that contained clumped or confluent platelets were removed to exclude them from the analysis. The final masks contained single platelets only and was used to calculate the single cell spreading area and ellipticity, i.e. the ratio of the long to the short axis of an equivalent ellipse.



The orientation of actin filaments was determined in two steps (Supplementary Fig. S2, step 1 to 3). First, F-actin images were independently processed by  $5 \times 5$  Sobel kernels of second order,  $S_{xx}$ ,  $S_{yy}$ , and  $S_{xy}$ , where  $x$  and  $y$  denote the gradient direction of the underlying first order kernels. To smoothen the gradient images, they were multiplied pixelwise by the corresponding smoothened F-actin intensity image and then Gaussian blurred with 4 pixel sigma. The local orientation for each pixel was then calculated by taking the quadrant-sensitive inverse tangent,  $\phi = 0.5 \tan^{-1}((2 I_{xy})/(I_{yy} - I_{xx}))$ . Second, features in F-actin images were enhanced by independently processing them by unsharp masking operations at smoothing degrees of 3, 5, 7, and 9 pixels, summation of the filtered images, and denoising them by a  $3 \times 3$  median filter. The resulting image was normalized to  $[0, 1]$  and thresholded at 0.08 to yield a fibre mask. For displaying the result (see Fig. 1c), the orientation between  $-\pi/2 \dots \pi/2$  was colour-coded in rainbow colours and pixels outside the fibre mask were set to black.

The local radial order within an actin image was calculated as follows (Supplementary Fig. S2, step 2 to 6). The centroid  $(x_0, y_0)$  for each cell was determined from the cell outline mask. The angle of the location of each pixel  $(x_i, y_i)$  within the outline relative to the centroid was calculated as  $\psi = \arctan((y_i - y_0)/(x_i - x_0))$ . The radial order of each pixel then results from the cosine between the orientation of the actin fibre and this angle,  $s_{radial} = 0.5 \cos(\phi - \psi) + 0.5$ . It ranged from 0 (actin fibre perpendicular to radial direction) to 1 (actin fibre aligned with radial direction). For displaying the result (see Fig. 1c), the radial order 0 ... 1 was colour-coded on a blue-white-red scale and pixels outside the fibre mask were set to black.

The fibre alignment per cell was given by the order parameter according to Zemel and co-workers<sup>23</sup> and calculated as follows. The mean orientation of fibres resulted from the mean angle (weighted by the actin intensity image, calculated in complex space) of all pixels that were in the fibre mask of a single cell:  $\phi_0 = \arg(\sum(\exp(i\phi) * \text{intensity}) / \sum(\text{intensity}))$ . Here,  $\arg$  gives the phase of the complex number. Then the difference between the local angle and the mean angle was computed  $\Delta\phi = \arg(\exp(i\phi) - \exp(i\phi_0))$ . Last, the degree of variation around the mean orientation was quantified by multiplying this difference by a factor of two, taking the cosine, calculating the intensity-weighted mean of all contributing pixels, which finally yields the fibre alignment:  $\sum(\cos(2\Delta\phi) * \text{intensity}) / \sum(\text{intensity})$ .

The radial order per cell was calculated by taking the intensity-weighted mean of the local order for all pixels in the fibre mask,  $\sum(s_{radial} * \text{intensity}) / \sum(\text{intensity})$ . The radial order lies between 0 (all fibres arranged in rings around the centroid) and 1 (all fibres radiate out from the centroid).

To visualize the characteristic morphologies of many platelets in a single plot, the radial distribution profile of the vinculin staining per cell was analysed as follows. The cell mask was divided into 20 angular sectors around its centroid. The intensities of all pixels in the vinculin image were summed up for each sector, divided by their total sum, and multiplied by 20. The result was plotted as a circumferential intensity profile (Fig. 1h). Here, values greater than 1 indicate sectors with a stronger-than-average staining and values smaller than 1 indicate directions with a weaker staining. This profile was fitted by a Fourier series up to fourth order,  $Y(\alpha) = 1 + \sum_{k=1}^4 a_k \cos(k\alpha) + b_k \sin(k\alpha)$ , where  $\alpha$  are the angles of the sectors relative to the centroid (see Supplementary Fig. S3b). The weights of the Fourier components were obtained from the fit as  $w_k = (a_k^2 + b_k^2)^{0.5}$ . Using these weights, each cell was then assigned a position  $(r, \varphi)$  in the overview plot (see Supplementary Fig. S3a). Here, the distance from the origin was given by the maximum amplitude minus a threshold,  $r = \max(Y) - 1.25$ , whereas the angle was calculated as  $\varphi = \arg(x_w + i y_w)$  with  $x_w = \sqrt{3}/2(w_3 - w_2)$  and  $y_w = w_4 - 0.5(w_2 + w_3)$ . Distances smaller than  $r = 0.33$  (inner circle in plot) were considered as isotropic; the larger the distances, the more pronounced was the bipolar or triangular arrangement. Finally, pooled positions from a whole platelet population were binned on a 0.02 grid, smoothened by a Gaussian, normalized to its maximum, and depicted as a contour plot (Supplementary Fig. S4).

**Statistics.** A comprehensive description of the statistical analysis is found in the Supplementary information. Briefly, boxes in boxplots represent upper and lower quartiles, notches depict the median and comparison intervals, the small circle marks the mean. Whiskers represent the 5<sup>th</sup> and 95<sup>th</sup> percentiles, and outside data are depicted as dots. A non-parametric Kruskal-Wallis rank test with Scheffe post-hoc testing was applied to make (multiple) comparisons as some parameters did not follow a normal distribution. As a general remark, Kruskal-Wallis was always less discriminative than ANOVA with Tukey-Kramer. The p-values for comparisons are reported and assumed to be significant for  $p < 10^{-4}$  (n.s.: not significant).

**Code availability.** MATLAB code, an example data set and a user guide are provided as electronic supplementary material that accompanies the online version of this article.

**Data availability.** The datasets generated during and/or analysed during the current study are available from the corresponding author on reasonable request.

## References

1. Lam, W. A. *et al.* Mechanics and contraction dynamics of single platelets and implications for clot stiffening. *Nat. Mater.* **10**, 61–66 (2011).
2. Schwarz Henriques, S., Sandmann, R., Strate, A. & Köster, S. Force field evolution during human blood platelet activation. *J. Cell Sci.* **125**, 3914–3920 (2012).
3. Myers, D. R. *et al.* Single-platelet nanomechanics measured by high-throughput cytometry. *Nat. Mater.* **16**, 230–235 (2016).
4. Lee, D., Fong, K. P., King, M. R., Brass, L. F. & Hammer, D. A. Differential dynamics of platelet contact and spreading. *Biophys. J.* **102**, 472–482 (2012).
5. Sandmann, R. & Köster, S. Topographic Cues Reveal Two Distinct Spreading Mechanisms in Blood Platelets. *Sci. Rep.* **6**, 22357 (2016).
6. Bearer, E. L., Prakash, J. M. & Li, Z. In *International Review of Cytology* **217**, 137–182 (2002).

7. McCarty, O. J. T. *et al.* Evaluation of the role of platelet integrins in fibronectin-dependent spreading and adhesion. *J. Thromb. Haemost.* **2**, 1823–33 (2004).
8. Nachmias, V. T. & Golla, R. Vinculin in relation to stress fibers in spread platelets. *Cell Motil. Cytoskeleton* **20**, 190–202 (1991).
9. Hagmann, J. Pattern formation and handedness in the cytoskeleton of human platelets. *Proc. Natl. Acad. Sci.* **90**, 3280–3283 (1993).
10. Aslan, J. E. *et al.* The PAK system links Rho GTPase signaling to thrombin-mediated platelet activation. *Am. J. Physiol. Cell Physiol.* **305**, C519–28 (2013).
11. Urban, A. E., Quick, E. O., Miller, K. P., Krcmery, J. & Simon, H.-G. Pdlim7 Regulates Arf6-Dependent Actin Dynamics and Is Required for Platelet-Mediated Thrombosis in Mice. *PLoS One* **11**, e0164042 (2016).
12. Tanaka, K. & Itoh, K. Reorganization of stress fiber-like structures in spreading platelets during surface activation. *J. Struct. Biol.* **124**, 13–41 (1998).
13. Burridge, K. & Wittchen, E. S. The tension mounts: Stress fibers as force-generating mechanotransducers. *J. Cell Biol.* **200**, 9–19 (2013).
14. Jirouskova, M., Jaiswal, J. K. & Collier, B. S. Ligand density dramatically affects integrin  $\alpha$ IIb  $\beta$ 3-mediated platelet signaling and spreading. *Blood* **109**, 5260–5269 (2007).
15. Haimovich, B., Lipfert, L., Brugge, J. S. & Shattil, S. J. Tyrosine phosphorylation and cytoskeletal reorganization in platelets are triggered by interaction of integrin receptors with their immobilized ligands. *J. Biol. Chem.* **268**, 15868–77 (1993).
16. Zhang, Y. *et al.* Platelet integrins exhibit anisotropic mechanosensing and harness piconewton forces to mediate platelet aggregation. *Proc. Natl. Acad. Sci.* **115**, 325–330 (2018).
17. Munnix, I. C. A., Cosemans, J. M. E. M., Auger, J. M. & Heemskerk, J. W. M. Platelet response heterogeneity in thrombus formation. *Thromb. Haemost.* **102**, 1149–56 (2009).
18. Feghhi, S. *et al.* Glycoprotein Ib-IX-V Complex Transmits Cytoskeletal Forces That Enhance Platelet Adhesion. *Biophys. J.* **111**, 601–608 (2016).
19. Carpenter, A. E. *et al.* CellProfiler: image analysis software for identifying and quantifying cell phenotypes. *Genome Biol.* **7**, R100 (2006).
20. Lukinavičius, G. *et al.* Fluorogenic probes for live-cell imaging of the cytoskeleton. *Nat. Methods* **11**, 731–733 (2014).
21. Wang, Y. *et al.* Force-activatable biosensor enables single platelet force mapping directly by fluorescence imaging. *Biosens. Bioelectron.* **100**, 192–200 (2018).
22. Blue, R., Murcia, M., Karan, C., Jirouskova, M. & Collier, B. S. Application of high-throughput screening to identify a novel  $\alpha$ IIb-specific small-molecule inhibitor of  $\alpha$ IIb $\beta$ 3-mediated platelet interaction with fibrinogen. *Blood* **111**, 1248–1256 (2007).
23. Zemel, A., Rehfeldt, F., Brown, A. E. X., Discher, D. E. & Safran, S. A. Optimal matrix rigidity for stress fiber polarization in stem cells. *Nat. Phys.* **6**, 468–473 (2010).
24. Théry, M. *et al.* Anisotropy of cell adhesive microenvironment governs cell internal organization and orientation of polarity. *Proc. Natl. Acad. Sci. USA* **103**, 19771–6 (2006).
25. Varga-Szabo, D., Pleines, I. & Nieswandt, B. Cell adhesion mechanisms in platelets. *Arterioscler. Thromb. Vasc. Biol.* **28**, 403–413 (2008).
26. Inoue, O. *et al.* Laminin stimulates spreading of platelets through integrin  $\alpha$ 6 $\beta$ 1-dependent activation of GPIIb. *Blood* **107**, 1405–1412 (2006).
27. Cho, J. & Mosher, D. F. Characterization of fibronectin assembly by platelets adherent to adsorbed laminin-111. *J. Thromb. Haemost.* **4**, 943–951 (2006).
28. Li, J. *et al.* RUC-4: A Novel  $\alpha$ IIb $\beta$ 3 Antagonist for Prehospital Therapy of Myocardial Infarction. *Arterioscler. Thromb. Vasc. Biol.* **34**, 2321–2329 (2014).
29. Burkhart, J. M. *et al.* The first comprehensive and quantitative analysis of human platelet protein composition allows the comparative analysis of structural and functional pathways. *Blood* **120**, e73–e82 (2012).
30. Zeiler, M., Moser, M. & Mann, M. Copy number analysis of the murine platelet proteome spanning the complete abundance range. *Mol. Cell. Proteomics* **13**, 3435–3445 (2014).
31. Zhu, J. *et al.* Closed headpiece of integrin  $\alpha$ IIb $\beta$ 3 and its complex with an  $\alpha$ IIb $\beta$ 3-specific antagonist that does not induce opening. *Blood* **116**, 5050–5059 (2010).
32. Negri, A., Li, J., Naini, S., Collier, B. S. & Filizola, M. Structure-based virtual screening of small-molecule antagonists of platelet integrin  $\alpha$ IIb $\beta$ 3 that do not prime the receptor to bind ligand. *J. Comput. Aided. Mol. Des.* **26**, 1005–1015 (2012).
33. Jiang, J. *et al.* A novel class of ion displacement ligands as antagonists of the  $\alpha$ IIb $\beta$ 3 receptor that limit conformational reorganization of the receptor. *Bioorg. Med. Chem. Lett.* **24**, 1148–1153 (2014).
34. Hantgan, R. R., Stahle, M. C., Connor, J. H., Connor, R. F. & Mousa, S. A.  $\alpha$ IIb $\beta$ 3 priming and clustering by orally active and intravenous integrin antagonists. *J. Thromb. Haemost.* **5**, 542–550 (2007).
35. Collier, B. S. & Shattil, S. J. The GPIIb/IIIa (integrin  $\alpha$ IIb  $\beta$ 3) odyssey: a technology-driven saga of a receptor with twists, turns, and even a bend. *Blood* **112**, 3011–3025 (2008).
36. Konradi, R., Acikgoz, C. & Textor, M. Polyoxyzolines for Nonfouling Surface Coatings - A Direct Comparison to the Gold Standard PEG. *Macromol. Rapid Commun.* **33**, 1663–1676 (2012).
37. Weydert, S. *et al.* Easy to Apply Polyoxyzoline-Based Coating for Precise and Long-Term Control of Neural Patterns. *Langmuir* **33**, 8594–8605 (2017).
38. Trichet, L. *et al.* Evidence of a large-scale mechanosensing mechanism for cellular adaptation to substrate stiffness. *Proc. Natl. Acad. Sci. USA* **109**, 6933–8 (2012).
39. Schoen, I., Pruitt, B. L. & Vogel, V. The Yin-Yang of Rigidity Sensing: How Forces and Mechanical Properties Regulate the Cellular Response to Materials. *Annu. Rev. Mater. Res.* **43**, 589–618 (2013).
40. Sun, Z., Guo, S. S. & Fässler, R. Integrin-mediated mechanotransduction. *J. Cell Biol.* **215**, 445–456 (2016).
41. Ghibaudo, M. *et al.* Traction forces and rigidity sensing regulate cell functions. *Soft Matter* **4**, 1836–1843 (2008).
42. Qiu, Y. *et al.* Platelet mechanosensing of substrate stiffness during clot formation mediates adhesion, spreading, and activation. *Proc. Natl. Acad. Sci. USA* **111**, 14430–14435 (2014).
43. Engler, A., Sheehan, M., Sweeney, H. L. & Discher, D. E. Substrate compliance vs ligand density in cell on gel responses. *Biophys. J.* **86**, 617–628 (2004).
44. Leon, C. *et al.* Megakaryocyte-restricted MYH9 inactivation dramatically affects hemostasis while preserving platelet aggregation and secretion. *Blood* **110**, 3183–3191 (2007).
45. Poulter, N. S. *et al.* Platelet actin nodules are podosome-like structures dependent on Wiskott-Aldrich syndrome protein and ARP2/3 complex. *Nat. Commun.* **6**, 7254 (2015).
46. van de Linde, S. *et al.* Direct stochastic optical reconstruction microscopy with standard fluorescent probes. *Nat. Protoc.* **6**, 991–1009 (2011).
47. Shroff, H. *et al.* Dual-color superresolution imaging of genetically expressed probes within individual adhesion complexes. *Proc. Natl. Acad. Sci.* **104**, 20308–20313 (2007).
48. Beach, J. R. *et al.* Actin dynamics and competition for myosin monomer govern the sequential amplification of myosin filaments. *Nat. Cell Biol.* **19**, 85–93 (2017).
49. Hu, S. *et al.* Long-range self-organization of cytoskeletal myosin II filament stacks. *Nat. Cell Biol.* **19**, 133–141 (2017).

50. Kenney, D. M. & Linck, R. W. The cytoskeleton of unstimulated blood platelets: structure and composition of the isolated marginal microtubular band. *J. Cell Sci.* **78**, 1–22 (1985).
51. White, J. G. & Sauk, J. Microtubule coils in spread blood platelets. *Blood* **64**, 470–478 (1984).
52. Bender, M. *et al.* Megakaryocyte-specific Profilin1-deficiency alters microtubule stability and causes a Wiskott–Aldrich syndrome-like platelet defect. *Nat. Commun.* **5**, 4746 (2014).
53. Simon, D., Kunicki, T. & Nugent, D. Platelet function defects. *Haemophilia* **14**, 1240–1249 (2008).
54. Ambo, H. *et al.* Three Novel Integrin  $\beta 3$  Subunit Missense Mutations (H280P, C560F, and G579S) in Thrombasthenia, Including One (H280P) Prevalent in Japanese Patients. *Biochem. Biophys. Res. Commun.* **251**, 763–768 (1998).
55. Xie, J., Pabón, D., Jayo, A., Butta, N. & González-Manchón, C. Type I Glanzmann thrombasthenia caused by an apparently silent  $\beta 3$  mutation that results in aberrant splicing and reduced  $\beta 3$  mRNA. *Thromb. Haemost.* **93**, 897–903 (2005).
56. Jennings, L. K. & White, M. M. Expression of ligand-induced binding sites on glycoprotein IIb/IIIa complexes and the effect of various inhibitors. *Am. Heart J.* **135**, S179–S183 (1998).
57. Zemel, A., Rehfeldt, F., Brown, A. E., Discher, D. E. & Safran, S. A. Cell shape, spreading symmetry and the polarization of stress-fibers in cells. *J Phys Condens Matter* **22**, 194110 (2010).
58. Ribeiro, A. J. S. *et al.* Contractility of single cardiomyocytes differentiated from pluripotent stem cells depends on physiological shape and substrate stiffness. *Proc. Natl. Acad. Sci. USA* **112**, 12705–12710 (2015).
59. Bray, M. A., Sheehy, S. P. & Parker, K. K. Sarcomere alignment is regulated by myocyte shape. *Cell Motil. Cytoskeleton* **65**, 641–651 (2008).
60. Kee, M. F., Myers, D. R., Sakurai, Y., Lam, W. A. & Qiu, Y. Platelet mechanosensing of collagen matrices. *PLoS One* **10**, 1–13 (2015).
61. Murrell, M., Oakes, P. W., Lenz, M. & Gardel, M. L. Forcing cells into shape: the mechanics of actomyosin contractility. *Nat. Rev. Mol. Cell Biol.* **16**, 486–498 (2015).
62. Früh, S. M., Schoen, I., Ries, J. & Vogel, V. Molecular architecture of native fibronectin fibrils. *Nat. Commun.* **6**, 7275 (2015).
63. Tse, J. R. & Engler, A. J. Preparation of hydrogel substrates with tunable mechanical properties. *Curr. Protoc. Cell Biol.* **10**, 1–16 (2010).

## Acknowledgements

We thank the GT patient M.T. for her consent and her time to participate in this study. We thank Prof. Barry S. Collier for insightful discussions and for generously providing the RUC compounds. We gratefully acknowledge Dr. Stefan Zürcher (SuSoS AG) for the generous gift of the non-fouling agents PAcAm-g-PMOXA and PLL-g-PEG. We thank Prof. J. Oldenburg and Dr. A Pavlova (Institute for Experimental Hematology, University Hospital Bonn) for performing the analysis of ITGA2B and ITGB3 genes. We would like to acknowledge Dr. Tanuj Sapra for helpful discussions and his initiative during the initial stage of the project, Dr. Jens Moeller and Dr. Lina Aires for assistance with hydrogels, Lukas Braun for preparing Supplementary Fig. S19, Dr. Isabel Gerber for assistance with EM preparation, and Dr. Tobias Schwarz and Joachim Hehl (ScopeM, ETH Zurich) for assistance with STED and SIM microscopes. We thank Dr. Jonas Ries (EMBL Heidelberg) for kindly providing software for the visualization of dSTORM data. This work was supported by a grant from the Swiss Science Foundation (CR32I3\_156931; V.V.), by the Wyss Zurich Translational Center (2-72187-16; V.V.), by ETH Zurich, and by RCSI (I.S.).

## Author Contributions

I.S., V.V. and O.M. laid out the concept of the study; S.L. and I.S. planned experiments; S.L. performed all platelet spreading experiments and confocal microscopy; I.S. performed live-cell imaging; S.L. and I.S. performed super-resolution imaging; S.S. performed cryo-ET; S.L. performed SEM; I.S. developed the image analysis scripts; S.L. prepared hydrogels; S.L. and I.S. analysed the data; J.D.S. recruited and characterized the GT patient; S.L. and I.S. drafted the manuscript; and all authors contributed to the interpretation of data and critically revised the report.

## Additional Information

**Supplementary information** accompanies this paper at <https://doi.org/10.1038/s41598-018-23684-w>.

**Competing Interests:** The authors declare no competing interests.

**Publisher's note:** Springer Nature remains neutral with regard to jurisdictional claims in published maps and institutional affiliations.



**Open Access** This article is licensed under a Creative Commons Attribution 4.0 International License, which permits use, sharing, adaptation, distribution and reproduction in any medium or format, as long as you give appropriate credit to the original author(s) and the source, provide a link to the Creative Commons license, and indicate if changes were made. The images or other third party material in this article are included in the article's Creative Commons license, unless indicated otherwise in a credit line to the material. If material is not included in the article's Creative Commons license and your intended use is not permitted by statutory regulation or exceeds the permitted use, you will need to obtain permission directly from the copyright holder. To view a copy of this license, visit <http://creativecommons.org/licenses/by/4.0/>.

© The Author(s) 2018